



High frequency ultrasound nonlinear scattering from porphyrin nanobubbles

Carly Pellow^{a,b,c,*}, Josephine Tan^{a,c}, Emmanuel Chérin^c, Christine E.M. Demore^{a,c}, Gang Zheng^{a,b}, David E. Goertz^{a,c}

^a Department of Medical Biophysics, University of Toronto, Toronto, ON M5G 1L7, Canada

^b Princess Margaret Cancer Research Centre, 101 College St., Toronto, ON M5G 0A3, Canada

^c Sunnybrook Research Institute, 2075 Bayview Avenue, Toronto, ON M4N 3M5, Canada

ARTICLE INFO

Keywords:

Nanobubble
Nonlinear scattering
High frequency
Multi-pulse schemes
Porphyrin
Imaging

ABSTRACT

Emerging contrast imaging studies have highlighted the potential of nanobubbles for both intravascular and extravascular applications. Reports to date on nanobubbles have generally utilized low frequencies (< 12 MHz), high concentrations ($> 10^9$ mL⁻¹), and B-mode or contrast-mode on preclinical and clinical systems. However, none of these studies directly examined nanobubble acoustic signatures systematically to implement nonlinear imaging schemes in a methodical manner based on nanobubble behaviour. Here, nanobubble nonlinear behaviour is investigated at high frequencies (12.5, 25, 30 MHz) and low concentration (10^6 mL⁻¹) in a channel phantom, with different pulse types in single- and multi-pulse sequences to examine behaviour under conditions relevant to high frequency imaging. Porphyrin nanobubbles are demonstrated to initiate nonlinear scattering at high frequencies in a pressure-threshold dependent manner, as previously observed at low frequencies. This threshold behaviour was then utilized to demonstrate enhanced nanobubble imaging with pulse inversion, amplitude modulation, and a combination of the two, progressing towards the improved sensitivity and expanded utility of these ultrasound contrast agents.

1. Introduction

Microbubble based ultrasound contrast imaging has been established for decades at conventional frequencies (~ 1 – 10 MHz). These microbubble agents are primarily comprised of bubbles 1 – 10 μm in diameter, filled with a high molecular weight gas and encapsulated with thin compliant shells to prolong their circulation time. After systemic injection, the primary basis for imaging is to detect and exploit distinct acoustic emissions occurring when the incident ultrasound pressure waves induce nonlinear bubble oscillations. Such oscillations occur more readily when bubbles are stimulated near their resonant frequencies, where the absolute levels of scattering are also enhanced. Microbubbles are of a size that fortuitously provides considerable nonlinear activity at diagnostic frequencies, and confines them to the vascular compartment [1,2].

Recently, there has been growing interest in submicron ultrasound cavitation agents on the order of tens to hundreds of nanometers. Their size permits them to gain access to the extravascular compartment of tumours [3] due to abnormal vessel permeability for extended imaging and therapeutic applications. They may also be present at higher

number densities within a focal volume relative to their larger microbubble counterparts, which may hold advantages for resolving microvessels [4]. Broadly, this class of submicron ultrasound contrast agents [3] includes nanobubbles (100–800 nm), echogenic liposomes (100 nm–1 μm), polymersomes (100 nm–1 μm), cavitation seeds (20–500 nm), and gas vesicles (45–250 nm diameter; 100–600 nm length). Here we focus on nanobubbles (NBs), a term generally used to describe encapsulated bubbles on the order of hundreds of nanometers. For NBs, the encapsulating layer holds additional benefits: Given their higher concentration within a focal volume [4] and higher surface area to volume ratio compared to microbubbles, the shell payload capacity can be drastically increased. There have thus been numerous approaches to formulating NBs with a variety of encapsulating components of lipids, polymers and proteins. Fabrication methodologies include manipulation of preformed microbubbles *via* filtration, differential centrifugation [5], acoustic conversion [6], or more direct approaches can be taken with alternative methods and shell components as size control excipients [7,8]. These formulations have been successfully utilized for both imaging [8–16] and therapeutic [17–22] applications: An influx of reports have emerged of NB use for

* Corresponding author at: Department of Medical Biophysics, University of Toronto, Toronto, ON M5G 1L7, Canada.

E-mail address: carly.pellow@mail.utoronto.ca (C. Pellow).

conventional ultrasound contrast imaging [9,14,15,23–27], targeted imaging [13,24,28], and as predictive markers [26,29]. There have been further compelling demonstrations of the therapeutic evidence of targeted [30–35] and loaded [20,21,30–37] NBs with both passive and active (ultrasound-triggered) approaches.

Imaging reports have generally employed either B-mode enhancement or the default contrast imaging mode on both high (12, 25 MHz [38,39]) and low (3–9 MHz [8–14,16]) frequency commercial systems. Typically, commercial contrast imaging modes involve multi-pulse sequences of pulse inversion (PI), amplitude modulation (AM), or the combination of the two (PIAM) [40–43]. With these approaches, differences in the amplitudes, frequency, and/or phase of the received signals from agent relative to tissue are exploited to improve the contrast to tissue ratio.

Despite this growing body of research, none of the studies to date have directly examined NB acoustic signatures systematically to methodically accomplish nonlinear imaging based on observed physical behaviour. NB imaging is notably challenging, as it relies on detection of acoustic signatures that are fundamentally impacted by the agent's small size. For sufficiently large unencapsulated bubbles, the Minnaert relationship holds, which indicates that a bubble's resonant frequency varies inversely with radius, r [44,45]. The presence of an encapsulating layer increases the resonant frequency and adds an additional viscous damping term proportional to $1/r^3$, introducing further nonlinearities in bubbles stimulated both on- or off-resonance [45,46], with the effects of damping (liquid and shell viscosities, thermal and acoustic) becoming more prominent as bubble size decreases. Ultimately, differences arise between the undamped and damped resonant frequency, at which the maximum radial oscillation occurs, and the frequency at which there is a maximum in backscatter [45,47]. Indeed, in an overdamped scenario there can be a loss of local maxima in the linear scattering peak.

While the details of NB shell properties remain to be well established, the application of linearized encapsulated bubble theory suggests a profound reduction in scattering as well as resonant frequencies in excess of those employed in biomedical ultrasound [4]. However, the feasibility of nonlinear NB imaging may arguably be due to two factors: First, many more NBs may be present in a given focal volume compared to microbubbles, and the population may offset individual bubble scattering differences [4]. Indeed, past studies typically employ high NB concentrations (10^9 – 10^{12} mL⁻¹). Second, the encapsulating layer plays a critical role in governing bubble acoustic response and can enhance nonlinear effects through strain-dependent rheological behaviour [48–51], facilitating the generation of nonlinear signals above a pressure threshold [4,52,53]. This is well established for phospholipid encapsulated bubbles on the order of 1–2 μ m insonated at diagnostic frequencies (< 5 MHz), where compression-dominated oscillations can be observed [54]. In this case, bubbles were stimulated below their resonant frequencies (of ~15–40 MHz for this size [47,55]) and could undergo nonlinear oscillations at pressures on the order of tens of kPa. Nonlinear bubble behaviour is also well established at higher ultrasound frequencies, with the majority of work being conducted with polydisperse commercial agents (Definity™, Micromarker™ [39,47,56,57]) and small bubble formulations [4,39,58,59]. It has been shown that nonlinear scattering occurs preferentially with smaller bubbles on the order of 1–2 μ m at 12 and 25 MHz transmit frequencies for phospholipid agents [39,60]. Interestingly, at 12 MHz compression-dominated oscillations occurred, whereas at 25 MHz expansion-dominated oscillations were prevalent.

Though NBs have not been assessed in this manner at high frequencies, we have recently shown that for transmit frequencies of 2.5 and 8 MHz, threshold-dependent scattering was observed for porphyrin-phospholipid encapsulated NBs, and accounted for in simulations by expansion-dominated oscillations [15]. This thresholding behaviour holds implications for AM imaging, and the prospect of utilizing submicron-sized bubbles to extend contrast imaging to higher

frequencies (> 10 MHz) has promise for intravascular ultrasound, superficial and ophthalmic imaging, and preclinical small-animal applications. Further, the bubbles utilized host high levels of porphyrin in the encapsulating layer. The inclusion of porphyrin photo/sonosensitizers conjugated to lipids in the bubble shell yields significant implications for optical and ultrasound based imaging and therapeutic applications [6,61,62]. In the present work, we investigate the acoustic response of porphyrin-phospholipid encapsulated NBs, with the objective of providing a rational basis for establishing appropriate imaging pulse sequences to expand the utility of submicron bubbles. To this end, we systematically study their fundamental, second harmonic, and subharmonic behaviour at high frequencies in response to single- and multi-pulse sequence (PI, AM, PIAM) schemes of various pulse types over a broad range of pressures.

2. Materials and methods

2.1. Agent preparation

Lipid films were prepared in 12 mm × 35 mm clear glass vials. A total of 0.5 mg of 30 mol % pyropheophorbide-lipid (synthesized by acylating 1-stearoyl-2-hydroxy-*sn*-glycero-3-phosphocholine with *Spirulina pacifica*-derived pyropheophorbide [61,63]), 60 mol % 1,2-distearoyl-*sn*-glycero-3-phosphocholine (DSPC) and 10 mol % 1,2-distearoyl-*sn*-glycero-3-phosphoethanolamine-N-[methoxy(polyethylene glycol)-2000] (DSPE-mPEG2k) were dissolved in chloroform. Samples were then dried under nitrogen gas while vortexing before being placed in a vacuum for 1 h. Films were then rehydrated with 1 mL of buffer solution comprised of 80 vol% phosphate buffered saline, 10 vol% propylene glycol, and 10 vol% glycerol. Vials were then heated above 70 °C, sonicated in a bath sonicator, and topped with octafluoropropane gas (C₃F₈, Fluoromed L.P.). Prior to experiments, samples were activated from room temperature by high shear gas dispersion with a VialMix (Lantheus Medical Imaging) for 45 s and passively cooled to room temperature over 10 min. The agent was then gently mixed and set to decant for 2 min prior to opening and extracting 0.5 mL from the bottom centre with a blunt 18 G needle. Agent was then diluted in 3 mL of phosphate buffered saline and passed through a 0.22 μ m pore size syringe filter (Millipore Millex-GV) to isolate the NB population. The agent size distribution was then measured with a 10 μ m aperture Coulter Counter (Multisizer 4e, Beckman-Coulter Inc.). The measured number (concentration) distribution mode was 0.24 μ m (Fig. 1a). NB studies typically report only the peak in the number distribution; however, in the context of gas-containing agents, larger particles typically dominate the acoustic response despite being of relatively lower number density. Thus, here we also report the volume distribution mode to be 0.28 μ m (Fig. 1b). Agent was used within 1 h after activation.

2.2. Phantom preparation

The phantom (Fig. 1d) consisted of a channel cast with a 17 G needle in an acrylic chamber (3 cm × 3 cm circular window cross-section, 1.15 cm thickness, 1 cm length) filled with 2% agar gel, held by mylar sheets. Following gelation, the needle was removed to create a channel (1.5 mm diameter) and mylar sheets were removed to minimize wall echoes.

2.3. Experimental apparatus and procedure

NB behaviour was observed at 10^6 bubbles per mL in the phantom and compared to that of linear scatterers (1 μ m polystyrene beads, Polysciences Inc.) to mimic tissue behaviour. The polystyrene beads were found to backscatter proportionally to f^d , in agreement with Faran's theory [64]. The phantom was positioned vertically in a tank filled with degassed, deionized water. The transducer focus was placed

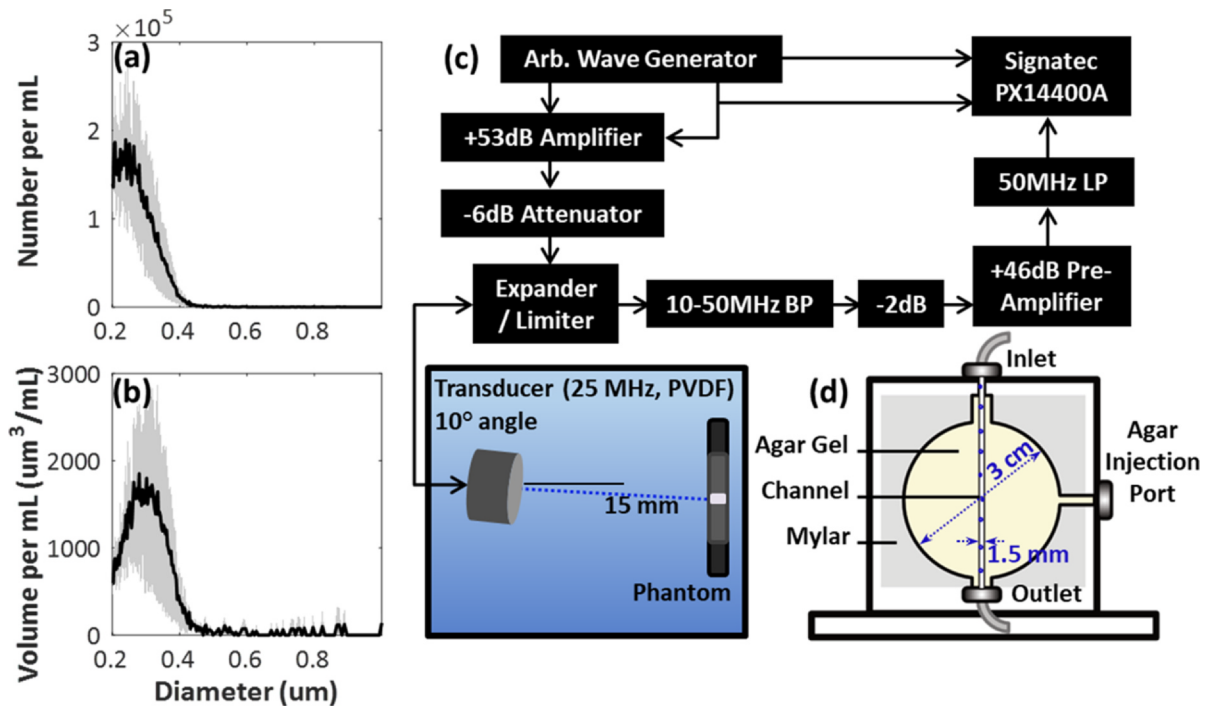


Fig. 1. Agent size distributions and schematic overview of the experimental configuration. (a) Number per mL (mode of $0.24 \mu\text{m}$) and (b) volume per mL ($\mu\text{m}^3/\text{mL}$) distributions (mode of $0.28 \mu\text{m}$) of porphyrin NBs, with standard deviations displayed as lighter shading around the mean. (c) Setup for pulse-echo benchtop cavitation measurements. (d) Channel phantom (1.5 mm diameter) intended to study agent in a large vessel-like geometry.

in the centre of the channel and oriented at a 10° angle to minimize reflections off the phantom faces (Fig. 1c). Fresh agent was brought into the focal zone and held stationary for each acquisition such that agent longevity under ultrasound exposure could be assessed, and confounding effects of motion would be removed.

An arbitrary waveform generator (Tektronix AWG5002) was used to drive a wideband PVDF transducer (VisualSonics RMV710, 25 MHz centre frequency, 15 mm focal length, F-number 2.1) at various transmit amplitudes. Generated peak pressures were measured at the focus using a calibrated 0.075 mm diameter needle hydrophone (model 2023, Precision Acoustics). The transducer was driven at 12.5 MHz, 25 MHz, and 30 MHz for enhanced receive sensitivity at the second harmonic, fundamental frequency, or subharmonic, respectively. Various pulse types (sinusoidal, cosine-tapered, and gaussian modulated waveforms) were investigated at each frequency over a range of 100–1000 kPa peak negative pressures in increments of 100 kPa, with $n = 3$ interrogations per pressure. Pulses from the arbitrary waveform generator were amplified with a 53-dB gated linear power amplifier (model # 3206, Herley-AMT), attenuated (-6 dB model # 24-6-34, DC to 8.5 GHz, 50 W, Aeroflex Weinschel) and transmitted through an expander to the transducer. Received echoes passed through a limiter, were bandpass filtered (10–50 MHz band-pass filter, 15542, Minicircuits), attenuated by 2-dB (Minicircuits), amplified with a 46-dB preamplifier (M/N AU 1313-94, Miteq Inc.), filtered (50 MHz low-pass filter, Minicircuits), and sampled at 400 MHz with a PC based 14-bit digitizer board (Signatec PX14400A, DynamicSignals LLC).

Single-pulse acquisitions (Fig. 2a) involved sending 10-cycle sinusoidal, 10-cycle with 20% cosine tapering, and 10, 25, and 50% bandwidth gaussian pulses. These pulses were sent at 1 kHz PRF for 100 bursts. Burst transmit amplitudes ranged from 100 to 1000 kPa peak negative pressures in increments of 100 kPa, with $n = 3$ interrogations per pressure. Multi-pulse acquisitions (Fig. 2b) involved sending 100 transmits of PI, AM, or PIAM pulse pairs constituted of either 5-cycle sinusoidal, 5-cycle with 20% cosine tapering, or 25, 50% bandwidth gaussian pulses at 40 kHz PRF. PI involves sending two consecutive pulses of inverted polarity, resulting in the removal of the linear

component of the scattered signal and conservation of even-order nonlinear components. This approach functions over the entire bandwidth of the received echoes, enhancing contrast and preserving spatial resolution [43]. In AM, echoes from two consecutive pulses of different amplitudes are scaled relative to each other by a factor corresponding to the inverse of the transmit amplitude ratio and subtracted, resulting in the removal of linear echoes and maintenance of even- and odd-order nonlinear components [65,66]. The combination of the two, PIAM, has also been utilized successfully to increase sensitivity to nonlinear responses and minimize linear echoes [42,43,67]. PI schemes investigated peak negative pressures from 100 to 1000 kPa in increments of 100 kPa, with $n = 3$ interrogations per pressure, at all three transmit frequencies. AM and PIAM schemes investigated pulses of amplitudes scaled by a factor of 2, starting with the larger amplitude pulse; i.e. 200–100 kPa, 400–200 kPa, 600–300 kPa, 800–400 kPa, 1000–500 kPa, with $n = 3$ interrogations per pressure set, for the centre transmit frequency of 25 MHz.

2.4. Data analysis

The acquired data was subsequently processed in MATLAB (MathWorks). Received signals were digitally filtered (10-MHz high-pass and 50-MHz low-pass; 5th order bandpass Butterworth filter) and combined according to Fig. 2b in the case of multi-pulse acquisitions. Resulting signals were then multiplied by a Hanning window of length matching the 5-cycle transmit pulse length at each frequency (400 ns at 12.5 MHz, 200 ns as 25 MHz, and 165 ns at 30 MHz) and centered on the channel axis. The windowed signal was zero-padded and Fourier transformed (frequency resolution: 4 kHz). A frequency bandwidth of -6 dB of the main lobe at each transmit was calculated. Power spectra were then integrated over that bandwidth centred on the fundamental and inertial cavitation bands for all transmit frequencies. The inertial cavitation band was defined to be between the fundamental and first ultraharmonic peaks for 12.5 and 25 MHz transmits (15.625 and 31.25 MHz respectively); and between the fundamental and subharmonic peak for the 30 MHz transmit (22.5 MHz). Additionally, for

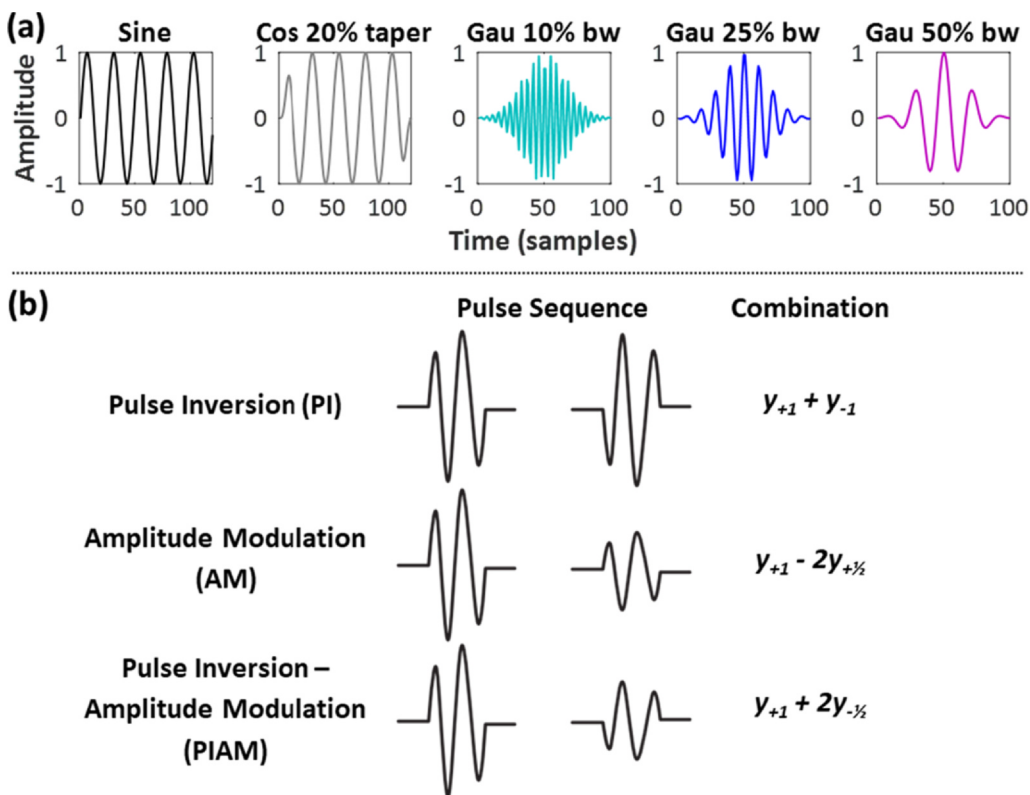


Fig. 2. Pulse types and multi-pulse modulation schemes. (a) Sample pulse types tested, including sinusoidal, 20% cosine-tapered, and 10%, 25%, and 50% bandwidth gaussian waves. (b) Multi-pulse sequences and received signal (y) combination for PI, AM, and PIAM, utilizing pulse types from (a) at 12.5, 25, and 30 MHz transmit frequencies.

the 12.5 and 30 MHz transmit frequencies, power spectra were also integrated over that bandwidth centred on the second harmonic and subharmonic peaks, respectively. The integrated powers corresponding to the first 10 transmit pulses were averaged (for each frequency band), and these averages were averaged again over all three interrogations performed at a given pressure. This was repeated for all transmit pressures. Results have not been compensated for the transducer frequency response but have been normalized with respect to the received integrated power at the maximum transmit pressure in the fundamental frequency band. For multi-pulse sequences, normalization occurs after pulse combination.

3. Results

3.1. Single-pulse sequence acquisitions

NBs and beads were first exposed to 12.5 MHz pulses to exploit the higher sensitivity of the transducer at the second harmonic on receive. Scattering results with a variety of single-pulse types (sinusoidal, 20% cosine tapered, 10 and 25% bandwidth gaussian) are shown in Fig. 3. Representative received power spectra (Fig. 3a) demonstrate the presence of fundamental and second and third harmonic peaks which increase as a function of pressure for all pulse types in both NB and bead cases. At higher pressures (> 500 kPa), NBs generate significant levels of signal between harmonics, most likely due to ultraharmonics associated with inertial cavitation. This supports the hypothesis of nonlinear scattering as well as inertial cavitation, and not merely linear scattering of second harmonic generated during nonlinear propagation (as in the case of beads). Power spectra were integrated over the fundamental, second harmonic, and inertial cavitation frequency bands as a function of pressure, comparing NB and bead scattering trends in Fig. 3b. At the fundamental and second harmonic frequency bands for all pulse types, a monotonic increase in received power was observed for beads while NBs generally demonstrate a rapid increase in scattered power followed by a plateau, with an inflection point at ~ 300 – 400 kPa.

The NBs also yielded a steady increase in inertial cavitation with increasing pressure, until plateauing at ~ 800 kPa.

Next the transducer was driven at 25 MHz for enhanced receive sensitivity at the fundamental frequency, and 30 MHz for higher receive sensitivity at the subharmonic frequency. Scattering results at 25 MHz (Fig. 4) and 30 MHz (Fig. 5) follow the same trends as at 12.5 MHz at the fundamental frequency and inertial bands. Distinct persistent fundamental signal is evident at both 25 and 30 MHz for all pulse types, while the 30 MHz transmit data additionally demonstrates a subharmonic peak for the NBs (absent from the bead data) at higher pressures for the sinusoidal, cosine-tapered, and 10% bandwidth gaussian pulses. The subharmonic peak however does not appear in the higher bandwidth gaussian pulse data, indicating limited utility of such pulse types for imaging via the subharmonic.

Agent longevity was then assessed at all frequencies and transmit pressures by investigating the variation in integrated power over successive pulse transmits (Fig. 6). A subset of pressures is overlaid to indicate relative signal longevity, demonstrating persistent nonlinear signals and sustained cavitation, indicated by high levels of integrated received power that remain fairly high as a function of successive bursts once above the threshold (~ 300 kPa). This was, however, accompanied by some agent destruction at higher pressures, visualized as decreases in integrated received power over successive bursts. We note that in some cases a rise in scattering can be observed in the latter 50 pulses. This is hypothesized to be due to disruption occurring within the proximal (transducer) side of the channel leading to a reduction of attenuation, and thereby resulting in increased received signal levels from NBs in the distal side. Representative full power spectra as a function of transmit number for 12.5, 25, and 30 MHz transmits are shown in Figs. A1, A2, A3, respectively.

The above single-pulse sequence cases at 12.5, 25, and 30 MHz transmits (Figs. 3–5) notably demonstrate that porphyrin NBs can oscillate nonlinearly at high frequencies. Further, the NBs qualitatively follow the same pressure-dependence trend seen previously at low transmit frequencies [15], demonstrating a pressure threshold above

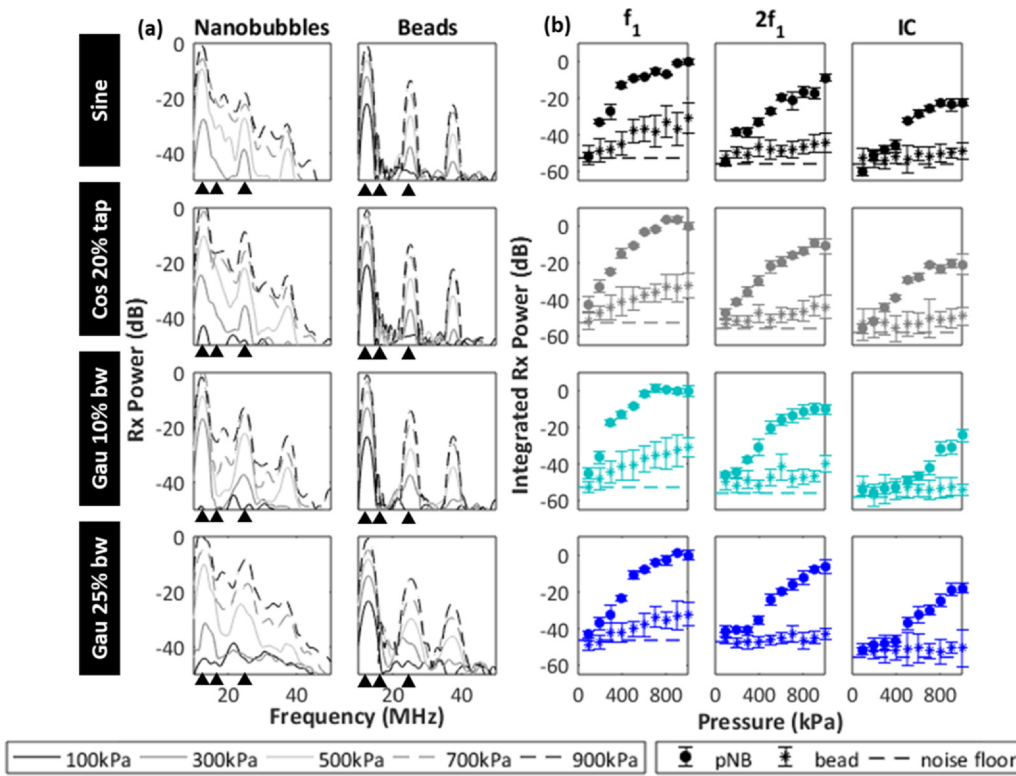


Fig. 3. Single-pulse sequence acquisitions at 12.5 MHz transmit frequency for several pulse types (row 1: sinusoidal 10-cycle, row 2: 20% cosine-tapered 10-cycle, row 3: gaussian 10% bandwidth, row 4: gaussian 25% bandwidth). (a) Received (Rx) power as a function of frequency for NBs and beads at several sample pressures. (b) Integrated received power as a function of pressure for NBs (solid circular markers) and beads (asterisk markers) over frequency bandwidths of 6 dB of the main lobe at the fundamental frequency (f_1), second harmonic ($2f_1$), and inertial cavitation (IC) regions (indicated with triangles). Data from $n = 3$ interrogations per pressure are averaged over the first 10 transmits and normalized to the received power at the fundamental frequency at the maximum transmit pressure.

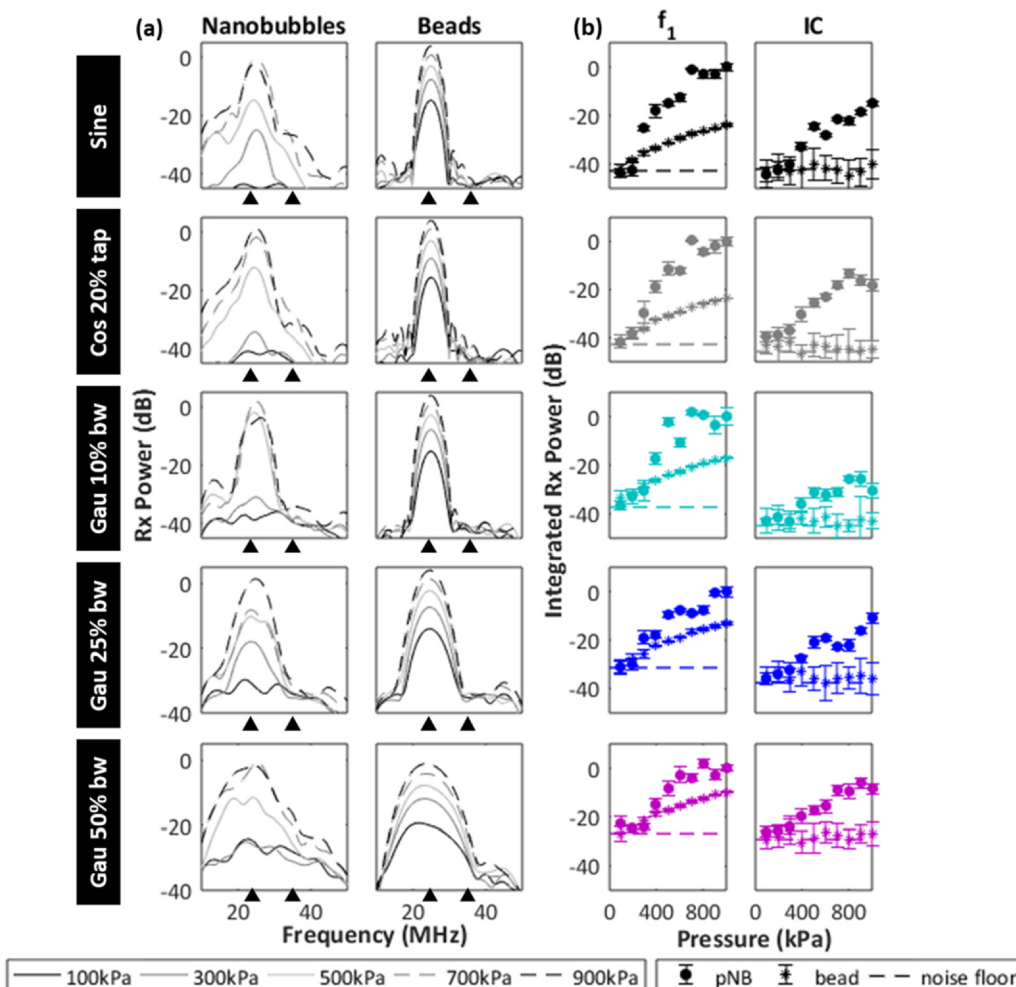


Fig. 4. Single-pulse sequence acquisitions at 25 MHz transmit frequency for several pulse types (row 1: sinusoidal 10-cycle, row 2: 20% cosine-tapered 10-cycle, row 3: gaussian 10% bandwidth, row 4: gaussian 25% bandwidth, row 5: gaussian 50% bandwidth). (a) Received (Rx) power as a function of frequency for NBs and beads at several sample pressures. (b) Integrated received power as a function of pressure for NBs (solid circular markers) and beads (asterisk markers) over frequency bandwidths of 6 dB of the main lobe at the fundamental frequency (f_1) and inertial cavitation (IC) bands (indicated with triangles). Data from $n = 3$ interrogations per pressure are averaged over the first 10 transmits and normalized to the received power at the fundamental frequency at the maximum transmit pressure.

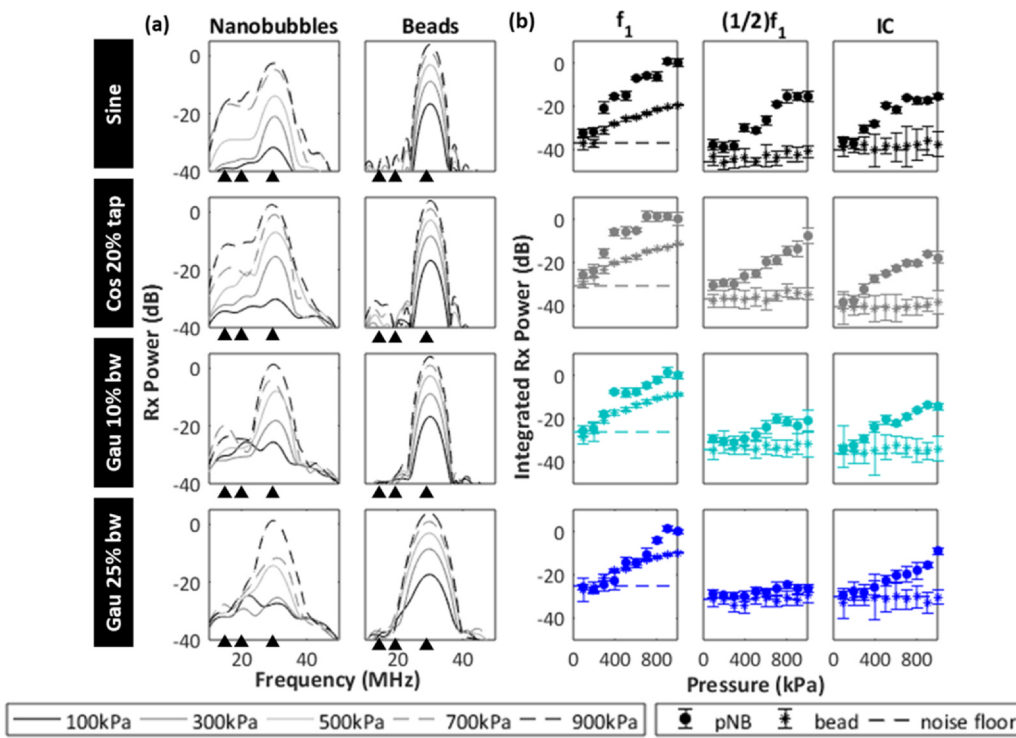


Fig. 5. Single-pulse sequence acquisitions at 30 MHz transmit frequency for several pulse types (row 1: sinusoidal 10-cycle, row 2: 20% cosine-tapered 10-cycle, row 3: gaussian 10% bandwidth, row 4: gaussian 25% bandwidth). (a) Received (Rx) power as a function of frequency for NBs and beads at several sample pressures. (b) Integrated received power as a function of pressure for NBs (solid circular markers) and beads (asterisk markers) over frequency bandwidths of 6 dB of the main lobe at the fundamental frequency (f_1), subharmonic ($1/2 f_1$), and inertial cavitation (IC) bands (indicated with triangles). Data from $n = 3$ interrogations per pressure are averaged over the first 10 transmits and normalized to the received power at the fundamental frequency at the maximum transmit pressure.

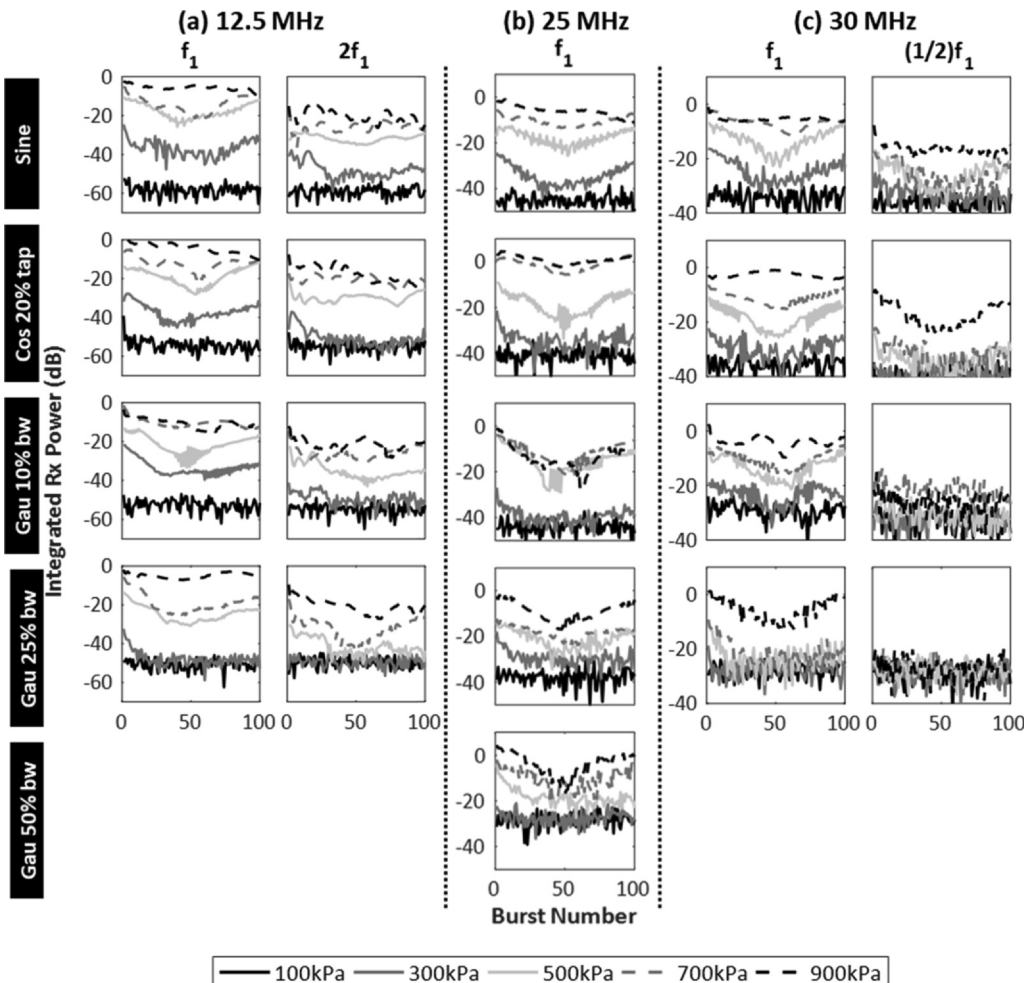


Fig. 6. Integrated received power as a function of successive ultrasound transmits for several pulse types (row 1: sinusoidal 10-cycle, row 2: 20% cosine-tapered 10-cycle, row 3: gaussian 10% bandwidth, row 4: gaussian 25% bandwidth, row 5: gaussian 50% bandwidth). (a) Fundamental (f_1) and second harmonic ($2f_1$) frequency bands at a 12.5 MHz transmit. (b) Fundamental frequency (f_1) band at 25 MHz. (c) Fundamental (f_1) and subharmonic ($1/2 f_1$) frequency bands at a 30 MHz transmit frequency. Data from $n = 3$ interrogations per pressure are averaged and normalized to the received power at the fundamental frequency at the maximum transmit pressure.

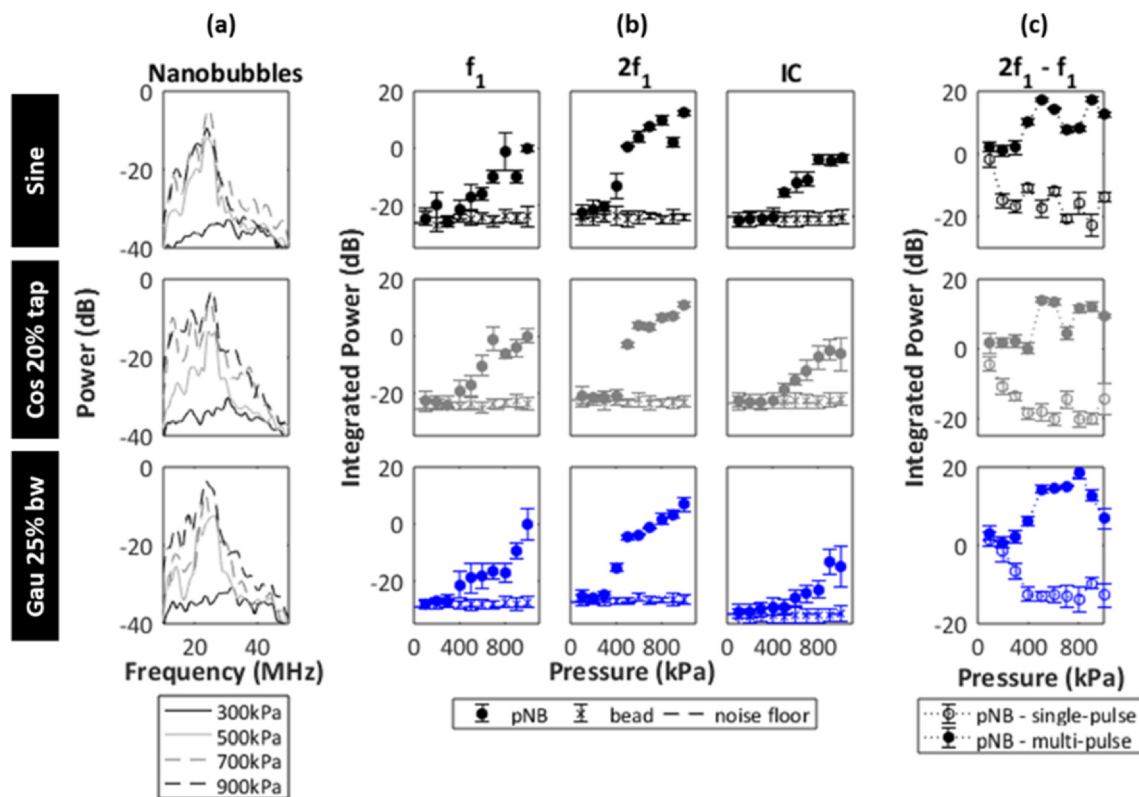


Fig. 7. PI at 12.5 MHz transmit frequency for several pulse types (row 1: sinusoidal 5-cycle, row 2: 20% cosine-tapered 5-cycle, row 3: gaussian 25% bandwidth). (a) Power as a function of frequency for NBs at several sample pressures. (b) Integrated power as a function of pressure for NBs (solid circular markers) and beads (asterisk markers) over frequency bandwidths of 6 dB of the main lobe at the fundamental frequency (f_1), second harmonic ($2f_1$), and inertial cavitation (IC) bands. (c) The difference between the second harmonic and fundamental frequency integrated power as a function of pressure for NBs during single-pulse (hollow marker) and multi-pulse (solid marker) acquisitions. Data from $n = 3$ interrogations per pressure and over the first 10 transmits are averaged and normalized (after pulse combination) to the received power at the fundamental frequency at the maximum transmit pressure.

which substantial nonlinear scatter ensued prior to plateauing. The nonlinearities are further shown to be persistent, with some agent destruction seen at higher pressures in subsequent ultrasound transmits, indicative of the onset of inertial cavitation.

3.2. Multi-pulse sequence acquisitions

NBs and beads were then subjected to multi-pulse sequence transmits (PI, AM, and PIAM), using the various pulse types at each transmit frequency, and across a range of pressures. Scattering results for the NBs and beads with a PI scheme at a transmit frequency of 12.5 MHz are shown in Fig. 7. As PI cancels odd harmonics and conserves even order responses, the fundamental and third harmonic peaks are drastically reduced while second harmonic peaks increase as a function of pressure (Fig. 7a). The second harmonic component had an apparent point of inflection at 400–500 kPa and thereafter increased strongly as a function of pressure (Fig. 7b). In Fig. 7c, the difference in scattered power between the second harmonic and fundamental frequency bands is plotted as a function of pressure for NBs comparing the single and dual pulsing schemes. In the single pulsing scheme, integrated scattered power at the second harmonic for the NBs lies consistently below the fundamental frequency, with both increasing in a similar fashion (Fig. 3). In the dual pulsing scheme (PI) for NBs, the fundamental frequency is reduced while the second harmonic is maintained, resulting in a positive difference that increases rapidly above threshold and plateaus at higher pressures. Conversely, the beads resulted in a linear increase in scattered power with increasing pressure in the single-pulse case (Fig. 3b; asterisk markers), and the PI scheme resulted in a reduction of linear signals to the noise floor (Fig. 7b; asterisk markers).

Scattering results for the NBs and beads with a PI scheme at transmit

frequencies of 25 and 30 MHz are shown in the [Supplemental Information](#) (Fig. A4, and Fig. A5). In both cases, the representative received power spectra demonstrate minimal fundamental frequency response due to cancellation of odd order harmonics as expected. The presence of broadband signal from NB scattering at higher pressures remains, however the elimination of the fundamental frequency band makes this pulsing scheme of little utility at 25 and 30 MHz for detecting scattering at lower pressures (i.e. in the absence of broadband signal). The 30 MHz pulses did result in a distinct subharmonic that increased as a function of pressure, however as in the single-pulse case (Fig. 5) the subharmonic did not appear in the higher bandwidth gaussian pulse data, resulting in limited potential utility for subharmonic NB imaging.

Scattering from NBs and beads with an AM scheme at a transmit frequency of 25 MHz are shown in Fig. 8a, b. Representative received power spectra (Fig. 8a) demonstrate a fundamental frequency response (maintained in AM) that increases as a function of pressure for the NBs. The AM scheme lends itself particularly well to the pressure threshold-dependent behaviour of NBs: In Fig. 8b, bead scattering data is reduced to noise level (~ 20 dB decrease compared to the single-pulse case in Fig. 4), while NB scattering above the noise floor is evident when the highest pressure in the pulsing scheme is above the threshold (i.e. > 400 kPa).

Scattering results for the NBs and beads with a PIAM scheme at a transmit frequency of 25 MHz are shown in Fig. 8c, d. Again, the representative received power spectra demonstrated a maintained fundamental frequency response that increased as a function of pressure for NBs once one pulse in the sequence exceeded the threshold (~ 400 – 500 kPa), while bead scattering was reduced to the noise floor. The rapid rise in scattered power at the fundamental frequency for NBs

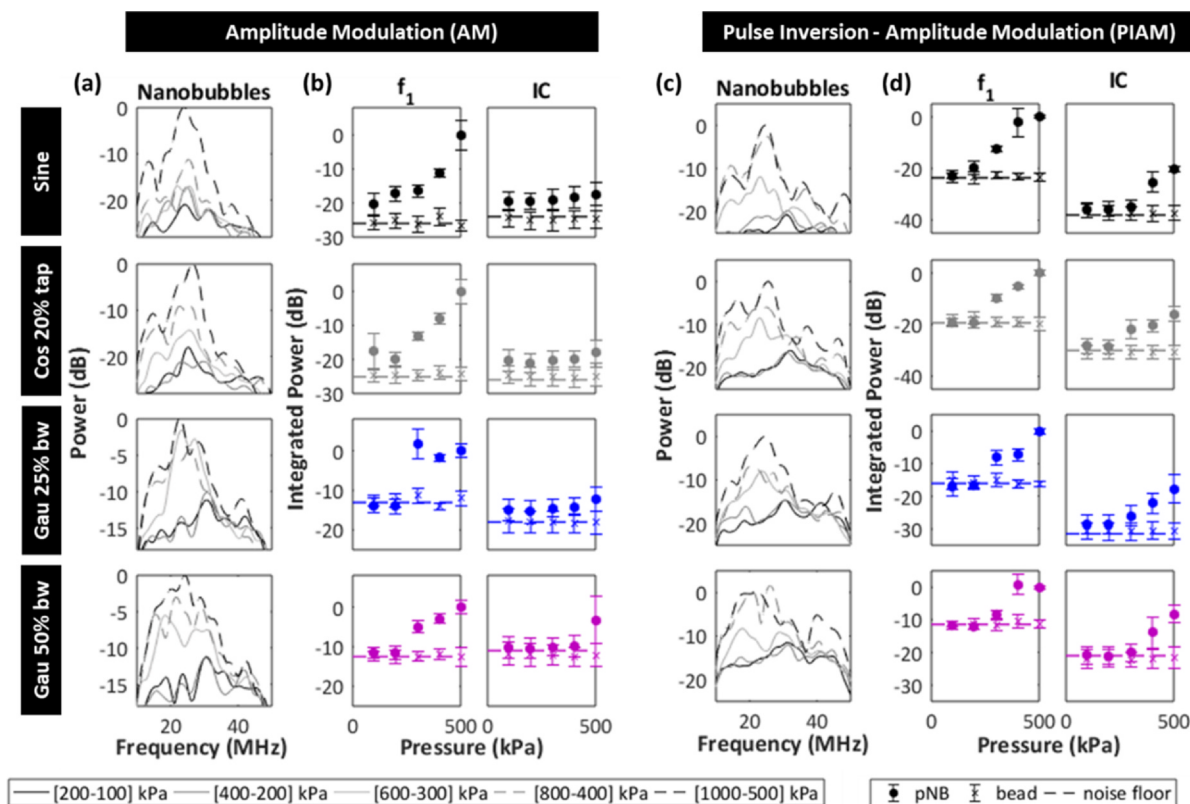


Fig. 8. AM and PIAM at 25 MHz transmit frequency for several pulse types (row 1: sinusoidal 5-cycle, row 2: 20% cosine-tapered 5-cycle, row 3: gaussian 25% bandwidth, row 4: gaussian 50% bandwidth). (a), (c) Received (Rx) power as a function of frequency for NBs at several sample pressures. (b), (d) Integrated received power as a function of pressure for NBs (solid circular markers) and beads (asterisk markers) over frequency bandwidths of 6 dB of the main lobe at the fundamental frequency (f_1) and inertial cavitation (IC) bands. Data from $n = 3$ interrogations per pressure and over the first 10 transmits are averaged and normalized (after pulse combination) to the received power at the fundamental frequency at the maximum transmit pressure.

was notably accompanied by low levels of inertial cavitation, particularly with AM. Representative full power spectra as a function of transmit number are shown in Fig. A6, demonstrating more broadband energy within the first few transmits at amplitude above threshold prior to diminishing after ~ 15 transmits, attributed to bubble destruction.

4. Discussion

Previous studies have demonstrated nonlinear scattering from 1 to 2 μm diameter bubbles [4,52,54,68] at low and high frequencies, and from submicron bubbles at low frequencies [8–16]. The present study demonstrates that porphyrin NBs can initiate nonlinear scattering at high transmit frequencies, and qualitatively follow similar apparent pressure-dependent thresholding previously observed at low frequencies [15]. This nonlinear threshold behaviour is further utilized to demonstrate enhanced NB detection with multi-pulse modulation schemes of PI, AM, and PIAM.

4.1. Pressure-dependent nanobubble oscillation at high frequency

As previously shown at lower frequencies (2.5 and 8 MHz) [15], the porphyrin NBs investigated in this study exhibit distinctly pressure-dependent activity at high frequencies. In particular there was an apparent threshold pressure for a rapid increase in scattering levels of ~ 20 dB (on average for different pulse types) occurring between 200 and 400 kPa at transmit frequencies of 12.5, 25, and 30 MHz (Figs. 3–5). However, we note that at the higher driving frequencies tested here, the threshold is less distinct and exhibits a lower rapid increase in scattered power while occurring over a slightly lower pressure range than in [15]. Here we consider a narrow size distribution

of bubbles (number mode 0.24 μm , volume mode 0.28 μm) strictly below 0.5 μm , with a variance of 0.15 μm . The variance in bubble size may contribute to a diffuse threshold, however, the thresholding properties observed here likely have a stronger dependence on frequency.

At low frequencies (2.5 and 8 MHz), the thresholding behaviour was accounted for by considering nonlinear shell rheology. Specifically, two scenarios were examined: initial surface tensions close to buckling with pressure-dependent behaviour associated with compression-dominated oscillations, or initial surface tensions close to rupture with expansion-dominated oscillations. The latter was posited as it was consistent with experimental results [15]. Effectively, the NBs were being insonated far below their expected resonant frequency and appeared to act as cavitation seeds, albeit ones that could act in a fairly persistent manner over successive pulses prior to destruction at high pressures. Shown in the present study, expansion-dominated oscillations may also be a factor in reducing agent stability, resulting in bubble destruction at higher pressures (Fig. 6), as gas/liquid interfaces would be exposed during expansion to permit diffusion. However, the relevant mechanism in play under these exposure conditions remains to be established.

With decreasing bubble size, the attenuation peak has been shown to broaden and increase in frequency [47,69]. For example, Definity™ size-isolated to 2 μm and 1 μm peak sizes resulted in broader attenuation peaks that rose to 15 and 40 MHz, respectively [47]. From these measurements of attenuation and size, linearized shell properties can be derived. For phospholipid encapsulated agents, it has been shown that with increasing frequency (4–19 MHz), shell stiffness increases slightly (1.53 to 1.76 N/m) while shell viscosity decreases substantially (0.29×10^{-6} to 0.08×10^{-6} kg/s) [69]. This trend is supported by single bubble optical and acoustic spectroscopy at lower

and higher frequency ranges [70–72]. The previous low frequency NB study's simulation parameter-space indicated that decreasing shell viscosity would result in the initial rapid increase in scattered power being shifted to lower pressures [15], as shown experimentally in the current study. However, these approaches estimate shell properties at the bubble resonance frequency, thus there is no decoupling of size and frequency effects.

The attenuation resonant behavior of NBs has not been assessed, but existing data from the aforementioned studies suggest resonant frequencies in excess of 50 MHz. If we utilize Definity™ properties (shell stiffness 1.71 N/m and shell friction 0.015×10^{-6} kg/s; measured over 12–28 MHz), a linear-regime estimate of the damped resonant frequency of phospholipid encapsulated NBs (300 nm) would be approximately 60 MHz (following the de Jong model [71]). Moreover, accounting for the increased shell stiffness due to the presence of porphyrin in the shell (found to be $3\text{--}5 \times$ stiffer than commercial microbubbles Definity™, SonoVue™, and Sonazoid™; shell stiffness 5.32 N/m; shell friction 0.19×10^{-6} kg/s [62]), this estimate would be heightened to 90 MHz. It is important to note with regards to these estimates that relationships between bubble size, exposure parameters and resultant bubble dynamics are complex: It has been proposed that the dependencies are related to rheological properties of the encapsulating shell [47,49,50,71], which in turn are functions of bubble size [71,73,74] and frequency of exposure [53,60,69]. The extent to which these encapsulating shell properties are inherently dependent on resting size or resonant size (i.e. dependent on exposure parameters and instantaneous radius) in the NB size range has yet to be determined. Further, while a reduction in bubble size is associated with increased resonant frequency, eventually the system is predicted to become overdamped with a loss of a distinct resonance peak [45,47]. Currently the resonant properties of NBs are unclear, and an interrogation of whether such a loss of resonance occurs is of interest.

Aside from considering linearized resonance that is associated with small amplitude insonation, it must also be considered that at higher amplitudes the resonant frequency peak (i.e. the frequency of maximum radial oscillations) is shifted to lower frequencies. This is well known in the context of unencapsulated bubbles and has been shown with phospholipid encapsulated agents $> 1 \mu\text{m}$ in size at low [53] and intermediate (up to 12 MHz) [72] frequencies. In these circumstances, asymmetric radial oscillations can occur [39,53,54] under the influence of nonlinear rheological behaviours of the shell such as strain-softening [52,53,75] and strain-hardening [60,76]. This phenomenon may be central to the process of initiating nonlinear signals from NBs at low and high frequencies. Here we do not attempt to reconcile NB behaviour at high frequencies as being distinctly due to agent size, shell properties, or exposure parameters, which remain coupled. Rather, we have shown that nonlinear effects clearly occur and that at appropriate pressure levels, pulsing schemes relevant to contrast imaging can preferentially retain signals relative to linear scatterers.

4.2. Nonlinear scattering with multi-pulse methods

In this study, sinusoidal, cosine tapered, and gaussian bandwidth modulated pulses were first compared as single transmitted pulses. Compared to a regular sinusoidal pulse, cosine tapering results in a reduction of the sidelobes in the frequency domain, resulting in improved contrast. Gaussian pulses of increasing bandwidth are of shorter duration, resulting in improved axial resolution and broadening of the main spectral lobe. As in Figs. 3–5, NBs demonstrated nonlinear scattering in response to each of these single-pulse types. However, the increasing linear scattering with pressure and increasing tissue harmonics (due to nonlinear propagation) with frequency (at fixed pressure) [77] limits imaging efforts, particularly given the generally lower scattering cross-section of smaller bubbles.

Multi-pulse sequences have been shown to increase the contrast-to-tissue ratio, at least in the context of microbubbles [40–43]. PI at

12.5 MHz transmit (Fig. 7) significantly enhanced 2nd harmonic contrast, however, cancellation of odd order harmonics renders this scheme of lower utility as frequency increases given limited depth penetration. For short pulses, the odd harmonics in PI may also not fully cancel, due to potential differences in transient bubble oscillations. The AM scheme lends itself particularly well to the pressure threshold-dependent behaviour exhibited by NBs, as it partially retains both even and odd order harmonics. Although linear echoes at the fundamental frequency cancel, residual nonlinear fundamental energy is retained (Fig. 8) and can be more useful than higher order harmonics when considering transmit bandwidth limitations, nonlinear propagation of higher harmonics, and frequency-dependent attenuation. PIAM (Fig. 8) results in the same fundamental amplitude as AM, as the coefficients contributing to the fundamental in both techniques are mathematically identical.

The longevity studies have shown that the measured nonlinearities persisted both in single-pulse (Fig. 6, Fig. A1, A2, A3) and multi-pulse (Fig. A6) sequence schemes. This implies that the non-zero PI, AM, and PIAM signals are not simply due to bubble destruction between pulses in the multi-pulse sequence, but rather arise, at least in part, due to nonlinear bubble responses (in the form of phase, amplitude, frequencies, or transients). Previous studies of pressure-dependent nonlinear microbubble [52,53,78,79] and NB [15] response have shed insight into the success of AM and PIAM imaging schemes. Though not directly investigated, it is possible that AM and PIAM schemes implemented on commercial scanners may be the rationale behind reports of successful NB imaging [7–10,12,14].

4.3. Perspectives: Future work and implications

The present study was completed under static conditions in one channel diameter (1.5 mm). The purpose of this work was more basic in nature: To show that nonlinear scattering could occur and that such signals could be retained with pulsing schemes relevant to high frequency imaging, and thus bubble behaviour as a function of pulse number was investigated. Blood flow would affect scattering primarily by determining – in conjunction with beam dimensions and vessel orientation – how many pulses bubbles are exposed to, and whether bubble behaviour changes as a function of pulse number, dependent on exposure conditions. This remains to be expanded upon in future work. It is further notable that alternate boundary conditions are expected to impact bubble oscillations: It has been shown that microbubbles within smaller vessels ($< 50 \mu\text{m}$ diameter) experience higher damping, shifted resonance, complex flow patterns, and asymmetrical collapse when in close proximity to the vessel wall, in a manner dependent on the size and mechanical properties of the boundary [80–82]. Similarly, we have demonstrated in past work that NB behaviour changes when confined in a viscoelastic medium [15], though the nuances of NB behaviour in microvessels and surrounded by varying media has not been studied. Elucidating more complex NB activity under alternate boundary conditions is of great interest as future work, though it requires the challenging fabrication of smaller channel phantoms in conjunction with ultrafast-frame microscopy that additionally holds high spatial resolution. Likewise, employing the nonlinear schemes from the present work in an array-based system would enable this NB scattering study to be extended to an imaging one. In this context the feasibility of leveraging NB pressure-threshold behaviour can be directly assessed *in vivo* and thus in vessels of varying sizes and properties, as well as under flow conditions. Such *in vivo* imaging will also offer and opportunity for comparing the performance of NBs with microbubbles.

Further, although the work here is limited to porphyrin encapsulated NBs, other nanoscale ultrasound contrast agent classes may similarly be candidates for improved imaging via multi-pulse schemes founded in their basic acoustic behaviour. Echogenic liposomes have demonstrated second harmonic emissions [83], and polymersomes have been found to elicit subharmonics [84], at least at low frequencies. Nanocup cavitation seeds have exhibited cavitation at high pressures

(> 1.5 MPa) [85], and gas vesicles have elicited pressure-dependent fundamental and second harmonic scattering at high frequencies [86]. Indeed, the pressure-dependent nonlinear response of gas vesicles has already been leveraged for AM imaging [87–89].

The wide variety of nanoscale ultrasound contrast agents affords structural versatility and intrinsic multifunctionality. The bubbles in this study contain porphyrin photosensitizers conjugated to lipids in the encapsulating layer, extending the conventional ultrasound contrast agent into a multimodal tool with fluorescence and photoacoustic imaging [6,61,62] as well as photodynamic, photothermal, and sonodynamic therapeutic capabilities [6]. Few studies to date have developed the subtle relationships between shell properties, structure, and behaviour for bubbles under different ultrasound conditions [39,53,69,90,91]. Continued understanding and leveraging of the basic physical behaviour of NBs and other nanoscale ultrasound contrast agents will further advance the field towards high resolution and extravascular applications.

5. Conclusion

Previous studies have reported NB imaging, though generally at low frequencies, high concentrations, and in B-mode and contrast mode on preclinical and clinical systems. However, none of these studies directly examined NB acoustic signatures systematically to provide a rational basis for establishing appropriate imaging pulse sequences. Here, the feasibility of improving NB nonlinear imaging was investigated with different pulse types in single- and multi-pulse schemes at high frequencies and low concentrations. Porphyrin NBs were found to initiate nonlinear scattering at high frequencies, qualitatively following the same pressure-dependence observed previously at low frequencies [15]. This threshold behaviour was then utilized to demonstrate enhanced NB imaging with multi-pulse schemes, particularly improved with AM and PIAM. Overall, this work moves towards expanding the utility of ultrasound contrast agents to higher frequency ranges and smaller sizes by directly studying NB behaviour in a systematic manner, and then working to establish effective imaging pulse sequences based on their physical behaviour.

CRedit authorship contribution statement

Carly Pellow: Conceptualization, Methodology, Software, Validation, Formal analysis, Investigation, Writing - original draft, Visualization. **Josephine Tan:** Software, Validation, Investigation. **Emmanuel Chérin:** Methodology, Writing - review & editing. **Christine E.M. Demore:** Writing - review & editing. **Gang Zheng:** Writing - review & editing, Supervision. **David E. Goertz:** Conceptualization, Methodology, Writing - review & editing, Supervision.

Declaration of Competing Interest

The authors declare that they have no known competing financial interests or personal relationships that could have appeared to influence the work reported in this paper.

Acknowledgements

The authors thank Michael Pozzobon for machining the phantom chamber used in this work. This work was supported by Prostate Cancer Canada, Canada Research Chairs Program, Canadian Institutes for Health Research, Natural Sciences and Engineering Research Council of Canada, Terry Fox Research Institute, Canada Foundation for Innovation, the Princess Margaret Cancer Foundation, and the Vanier Canada Graduate Scholarship.

Appendix A. Supplementary material

Supplementary data to this article can be found online at <https://doi.org/10.1016/j.ultras.2020.106245>.

References

- [1] M. Kurt, K. Shaikh, L. Peterson, K. Kurrelmeyer, G. Shah, S. Nagueh, R. Fromm, M. Quinones, W. Zoghbi, Impact of contrast echocardiography on evaluation of ventricular function and clinical management in a large prospective cohort, *J. Am. Coll. Cardiol.* 53 (2009) 802–810.
- [2] S. Wilson, P. Burns, Microbubble-enhanced US in body imaging: What role? *Radiology* 257 (2010) 24–39.
- [3] C. Pellow, D.E. Goertz, G. Zheng, Breaking free from vascular confinement: status and prospects for submicron ultrasound contrast agents, *WIREs Nanomed. Nanobiotechnol.* e1502 (2017).
- [4] D.E. Goertz, M.E. Frijlink, N. de Jong, A.F.W. van der Steen, High frequency non-linear scattering from a micrometer to submicrometer sized lipid encapsulated contrast agent, *Ultrasound Med. Biol.* 32 (4) (2006) 569–577.
- [5] J.A. Feshitan, C.C. Chen, J.J. Kwan, M.A. Borden, Microbubble size isolation by differential centrifugation, *J. Colloid Interface Sci.* 329 (2009) 316–324.
- [6] E. Huynh, B.Y.C. Leung, B.L. Helfield, M. Shakiba, J.-A. Gandier, C.S. Jin, E.R. Master, B.C. Wilson, D.E. Goertz, G. Zheng, In situ conversion of porphyrin microbubbles to nanoparticles for multimodality imaging, *Nat. Nanotechnol.* 10 (4) (2015) 325–332.
- [7] T.M. Krupka, L. Solorio, R.E. Wilson, H. Wu, N. Azar, A.A. Exner, Formulation and characterization of echogenic lipid-pluronic nanobubbles, *Mol Pharm* 7 (1) (2010) 49–59.
- [8] W.B. Cai, H.L. Yang, J. Zhang, J.K. Yin, Y.L. Yang, L. Zhang, Y.Y. Duan, The optimized fabrication of nanobubbles as ultrasound contrast agents for tumor imaging, *Sci. Rep.* 5 (2015).
- [9] T. Yin, P. Wang, R. Zheng, B. Zheng, D. Cheng, X. Zhang, X. Shuai, Nanobubbles for enhanced ultrasound imaging of tumors, *Int. J. Nanomed.* 7 (2012) 895–904.
- [10] H. Wu, N.G. Rognin, T.M. Krupka, L. Solorio, H. Yoshiara, G. Guenette, C. Sanders, N. Kamiyama, A.A. Exner, Acoustic characterization and pharmacokinetic analyses of new nanobubble ultrasound contrast agents, *Ultrasound Med. Biol.* 39 (11) (2013) 2137–2146.
- [11] Z. Xing, J. Wang, H. Ke, B. Zhao, X. Yue, Z. Dai, J. Liu, The fabrication of novel nanobubble ultrasound contrast agent for potential tumor imaging, *Nanotechnology* 21 (2010).
- [12] R.H. Perera, H. Wu, P. Peiris, C. Hernandez, A. Burke, H. Zhang, A.A. Exner, Improving performance of nanoscale ultrasound contrast agents using N, N-dimethylacrylamide stabilization, *Nanomed.: Nanotechnol. Biol. Med.* 13 (2017) 59–67.
- [13] H. Yang, W. Cai, L. Xu, X. Lv, Y. Qiao, P. Li, H. Wu, Y. Yang, L. Zhang, Y. Duan, Nanobubble-affibody: Novel ultrasound contrast agents for targeted molecular ultrasound imaging of tumor, *Biomaterials* 37 (2014) 279–288.
- [14] M.A. Wheatley, J. Lewandowski, Nano-sized ultrasound contrast agent: salting-out method, *Mol. Imag.* 9 (2) (2010) 96–107.
- [15] C. Pellow, C. Acconcia, G. Zheng, D.E. Goertz, Threshold-dependent nonlinear scattering from porphyrin nanobubbles for vascular and extravascular applications, *Phys. Med. Biol.* 63 (21) (2018).
- [16] M. Shang, K. Wang, L. Guo, S. Duan, Z. Lu, J. Li, Development of novel ST68/PLA-PEG stabilized ultrasound nanobubbles for potential tumor imaging and theranostic, *Ultrasonics* 99 (2019) 1056947.
- [17] R.H. Perera, L. Solorio, H. Wu, M. Gangolli, E. Silverman, C. Hernandez, P.M. Peiris, A.-M. Broome, A.A. Exner, Nanobubble ultrasound contrast agents for enhanced delivery of thermal sensitizer to tumors undergoing radiofrequency ablation, *Pharm. Res.* 31 (2014) 1407–1417.
- [18] X. Xie, W. Lin, H. Liu, J. Deng, Y. Chen, H. Liu, F. Xudong, Y. Yang, Ultrasound-responsive nanobubbles contained with peptide-campothecin conjugates for targeted drug delivery, *Drug Deliv.* 23 (8) (2016) 2756–2764.
- [19] B. Wu, Q. Qiao, X. Han, H. Jing, H. Zhang, H. Liang, W. Cheng, Targeted nanobubbles in low-frequency ultrasound-mediated gene transfection and growth inhibition of hepatocellular carcinoma cells, *Tumor Biol.* 37 (2016) 12113–12121.
- [20] R. Cavalli, A. Bisazza, P. Giustetto, A. Civra, D. Lembo, G. Trotta, C. Guiot, M. Trotta, Preparation and characterization of dextran nanobubbles for oxygen delivery, *Int. J. Pharm.* 381 (2009) 160–165.
- [21] C.-H. Fan, H.-L. Liu, C.-Y. Ting, Y.-H. Lee, C.-Y. Huang, Y.-J. Ma, K.-C. Wei, T.-C. Yen, C.-K. Yeh, Submicron-bubble-enhanced focused ultrasound for blood brain barrier disruption and improved CNS drug delivery, *PLoS One* 5 (2014) 9.
- [22] N. Matsuura, E. Koonar, S. Zhu, B.Y. Leung, M. Seo, N. Sivapalan, D.E. Goertz, Inducing antivasculature effects in tumors with ultrasound stimulated micron-sized bubbles, *IEEE Int. Ultrason. Symp.* (2015).
- [23] A. de Leon, R. Perera, C. Hernandez, M. Cooley, O. Jung, S. Jeganathan, E. Abenojar, G. Fishbein, A. Jafari Sojehrood, C.C. Emerson, P.L. Stewart, M.C. Kolios, A.A. Exner, Contrast enhanced ultrasound imaging by nature-inspired ultrastable echogenic nanobubbles, *Nanoscale* 11 (33) (2019) 15647–15658.
- [24] J. Zhang, L. Wei, Y. Zhao, Synthesis of nanobubbles for improved ultrasound tumor-imaging applications, *3 Biotech* 10 (12) (2019) 1–6.
- [25] C. Hernandez, J. Lilly, P. Nittayacharn, J. Hadley, R. Coyne, M.C. Kolios, A.A. Exner, Ultrasound signal from sub-micron lipid-coated bubbles, 2017 IEEE International Ultrasonics Symposium (IUS), Washington, DC, (2017).
- [26] R. Liu, J. Tang, Y. Xu, Z. Dai, Bioluminescence imaging of inflammation in vivo based on bioluminescence and fluorescence resonance energy transfer using

- nanobubble ultrasound contrast agent, *ACS Nano* 13 (5) (2019) 5124–5132.
- [27] S.A. Peyman, J.R. McLaughlin, R.H. Abou-Saleh, G. Marston, B.R.G. Johnson, S. Freear, P.L. Coletta, A.F. Markham, S.D. Evans, On-chip preparation of nanoscale contrast agents towards high-resolution ultrasound imaging, *Lab Chip* 16 (2016) 679–687.
- [28] Y. Gao, C. Hernandez, H.-X. Yuan, J. Lilly, P. Kota, H. Zhou, H. Wu, A.A. Exner, Ultrasound molecular imaging of ovarian cancer with CA-125 targeted nanobubble contrast agents, *Nanomedicine* 13 (7) (2017) 2159–2168.
- [29] D.G. Ramirez, E. Abenojar, C. Hernandez, D.S. Lorberbaum, L.A. Papazian, S. Passman, V. Pham, A.A. Exner, R.K.P. Benninger, Contrast-enhanced ultrasound with sub-micron sized contrast agents detects interstitialitis in mouse models of type1 diabetes, *Nat. Commun.* 11 (2020) 1–13.
- [30] F. Bosca, P.A. Bielecki, A.A. Exner, A. Barge, Porphyrin-loaded Pluronic nanobubbles: A new ultrasound-activated agent for future theranostic applications, *Bioconjug. Chem.* 29 (2) (2018) 234–240.
- [31] M. Wu, H. Zhao, L. Guo, Y. Wang, J. Song, X. Zhao, C. Li, L. Hao, D. Wang, J. Tang, Ultrasound-mediated nanobubble destruction (UMND) facilitates the delivery of A10-3.2 aptamer targeted and siRNA-loaded cationic nanobubbles for therapy of prostate cancer, *Drug Deliv.* 25 (1) (2018) 226–240.
- [32] C. Hu, M. Wu, R. Zhang, D. Jiang, J. Wang, Ultrasound-mediated nanobubble destruction (UMND) facilitates the delivery of VEGFR2-targeted CD-TK-loaded cationic nanobubbles in the treatment of bladder cancer, *J. Cancer Res. Clin. Oncol.* 146 (3) (2020) 1.
- [33] Z. Yu, Y. Wang, D. Xu, L. Zhu, M. Hu, Q. Liu, W. Lan, J. Jiang, L. Wang, G250 antigen-targeting drug-loaded nanobubbles combined with ultrasound targeted nanobubble destruction: A potential novel treatment for renal cell carcinoma, *Int. J. Nanomed.* 15 (2020) 81–95.
- [34] H. Kida, K. Nishimura, K. Ogawa, A. Watanabe, L.B. Feril, Y. Irie, H. Endo, S. Kawakami, K. Tachibana, Nanobubble mediated gene delivery in conjunction with a hand-held ultrasound scanner, *Front. Pharmacol.* 11 (2020) 363.
- [35] S. Zhong, Z. Ling, Z. Zhou, J. He, H. Ran, Z. Wang, Q. Zhang, W. Song, Y. Zhang, J. Luo, Herceptin-decorated paclitaxel-loaded poly(lactide-co-glycolide) nanobubbles: ultrasound-facilitated release and targeted accumulation in breast cancers, *Pharm. Dev. Technol.* 25 (4) (2019) 454–463.
- [36] P. Nittayacharn, H.-X. Yuan, C. Hernandez, P. Bielecki, H. Zhou, A.A. Exner, Enhancing tumor drug distribution with ultrasound-triggered nanobubbles, *J. Pharmaceut. Sci.* 108 (9) (2019) 3091–3098.
- [37] M. Argenziano, G. Banche, A. Luganini, N. Finesso, V. Allizond, G.R. Gulino, A. Khadjavi, R. Spagnolo, V. Tullio, G. Giribaldi, C. Guiot, A.M. Cuffini, M. Prato, R. Cavalli, Vancomycin-loaded nanobubbles: A new platform for controlled antibiotic delivery against methicillin-resistant *Staphylococcus Aureus* infections, *Int. J. Pharm.* 523 (1) (2017) 176–188.
- [38] E.C. Abenojar, P. Nittayacharn, A.C. de Leon, R. Perera, Y. Wang, I. Bederman, A.A. Exner, Effect of bubble concentration on the in vitro and in vivo performance of highly stable lipid shell-stabilized micro- and nanoscale ultrasound contrast agents, *Langmuir* 35 (2019) 10192–10202.
- [39] B.L. Helfield, E. Cherin, F.S. Foster, D.E. Goertz, Investigating the subharmonic response of individual phospholipid encapsulated microbubbles at high frequencies: a comparative study of five agents, *Ultrasound Med. Biol.* 38 (5) (2012) 846–863.
- [40] J.J. Hwang, D. Hope Simpson, Two pulse technique for ultrasonic harmonic imaging, US Patent 5951478, 14 September 1999.
- [41] D. Hope Simpson, C.T. Chin, P.N. Burns, Pulse inversion Doppler: a new method for detecting nonlinear echoes from microbubble contrast agents, *IEEE Trans. Ultrason. Ferroelectr. Freq. Control* 46 (2) (1999) 372–382.
- [42] P.J. Phillips, Contrast pulse sequences (CPS): Imaging nonlinear microbubbles, *IEEE Ultrason. Symp.* 2 (2001) 1739–1745.
- [43] R.J. Eckersley, C.T. Chin, P.N. Burns, Optimising phase and amplitude modulation schemes for imaging microbubble contrast agents at low acoustic power, *Ultrasound Med. Biol.* 31 (2) (2005) 213–219.
- [44] M. Minnaert, On musical air-bubbles and the sound of running water, *Phil. Mag.* 16 (104) (1933) 235–248.
- [45] D.B. Khismatullin, Resonance frequency of microbubbles: Effect of viscosity, *J. Acoust. Soc. Am.* (2004).
- [46] N. de Jong, L. Hoff, T. Skotland, N. Bom, Absorption and scatter of encapsulated gas filled microspheres: Theoretical considerations and some measurements, *Ultrasonics* 30 (1992) 95–103.
- [47] D.E. Goertz, N. de Jong, A.F.W. van der Steen, Attenuation and size distribution measurements of definitivity and manipulated definitivity populations, *Ultrasound Med. Biol.* 33 (9) (2007) 1376–1388.
- [48] P. Marmottant, S. van der Meer, M. Emmer, M. Versluis, A model for large amplitude oscillations of coated bubbles accounting for buckling and rupture, *J. Acoust. Soc. Am.* 118 (2005) 3499–3505.
- [49] A.A. Doinikov, J.F. Haac, P.A. Dayton, Modeling of nonlinear viscous stress in encapsulating shells of lipid-coated contrast agent microbubbles, *Ultrasonics* 49 (2) (2009) 269–275.
- [50] Q. Li, T.J. Matula, J. Tu, X. Guo, D. Zhang, Modeling complicated rheological behaviors in encapsulating shells of lipid-coated microbubbles accounting for non-linear changes of both shell viscosity and elasticity, *Phys. Med. Biol.* 58 (4) (2013) 985–998.
- [51] T. Faez, M. Emmer, K. Kooiman, M. Versluis, A. van der Steen, N. de Jong, 20 years of ultrasound contrast agent modeling, *IEEE Trans. Ultrason. Ferroelectr. Freq. Control* 60 (1) (2013) 7–20.
- [52] M. Emmer, A. van Wamel, D.E. Goertz, N. de Jong, The onset of microbubble vibration, *Ultrasound Med. Biol.* 33 (6) (2007) 941–949.
- [53] M. Overvelde, V. Garbin, J. Sijl, B. Dollet, N. de Jong, D. Lohse, M. Versluis, Nonlinear shell behavior of phospholipid-coated microbubbles, *Ultrasound Med. Biol.* 36 (12) (2010) 2080–2092.
- [54] N. de Jong, M. Emmer, C.T. Chin, A. Bouakaz, F. Mastik, D. Lohse, M. Versluis, “Compression-only” behavior of phospholipid-coated contrast bubbles, *Ultrasound Med. Biol.* 33 (4) (2007) 653–656.
- [55] D.E. Goertz, M.E. Frijlink, M.M. Voormolen, N. de Jong, A.F. van der Steen, High frequency attenuation measurements of lipid encapsulated contrast agents, *Ultrasonics* 44 (2006) e131–e134.
- [56] K. Cheung, O. Couture, P.D. Bevan, E. Cherin, R. Williams, P.N. Burns, F.S. Foster, In vitro characterization of the subharmonic ultrasound signal from Definity microbubbles at high frequencies, *Phys. Med. Biol.* 53 (5) (2008) 1209–1223.
- [57] D.E. Goertz, M. Frijlink, A. Bouakaz, C.T. Chin, N. de Jong, A.F.W. van der Steen, The effects of bubble size on nonlinear scattering from microbubbles, *Ultrasonics* 2 (2003) 1503–1506.
- [58] D.E. Goertz, M.E. Frijlink, N. de Jong, A.F.W. van der Steen, Nonlinear intravascular ultrasound contrast imaging, *Ultrasound Med. Biol.* 32 (2006) 491–502.
- [59] A. Needles, M. Arditi, N.G. Rognin, J. Mehi, T. Coulthard, C. Bilan Tracey, E. Gaud, P. Frinking, D. Hirson, F.S. Foster, Nonlinear contrast imaging with an array-based micro-ultrasound system, *Ultrasound Med. Biol.* 36 (2010) 2097–2106.
- [60] T. Faez, M. Emmer, M. Docter, J. Sijl, M. Versluis, N. de Jong, Characterizing the subharmonic response of phospholipid-coated microbubbles for carotid imaging, *Ultrasound Med. Biol.* 37 (6) (2011) 958–970.
- [61] E. Huynh, C.S. Jin, B.C. Wilson, G. Zheng, Aggregate enhanced trimodal porphyrin shell microbubbles for ultrasound, photoacoustic, and fluorescence imaging, *Bioconjug. Chem.* 25 (4) (2014) 796–801.
- [62] E. Huynh, J. Lovell, B.L. Helfield, M. Jeon, C. Kim, D.E. Goertz, B.C. Wilson, G. Zheng, Porphyrin shell microbubbles with intrinsic ultrasound and photoacoustic properties, *J. Am. Chem. Soc.* 134 (40) (2012) 16464–16467.
- [63] J.F. Lovell, C.S. Jin, E. Huynh, H. Jin, C. Kim, J.L. Rubinstein, W.C.W. Chan, W. Cao, L.V. Wang, G. Zheng, Porphyrin nanovesicles generated by porphyrin bilayers for use as multimodal biophotonic contrast agents, *Nat. Mater.* 10 (2011) 324–332.
- [64] J.F. F. Jr., Sound scattering by solid cylinders and spheres, *J. Acoust. Soc. Am.* 23 (4) 1951.
- [65] G. Brock-Fisher, M. Poland, P. Rafter, Means for increasing sensitivity in nonlinear ultrasonic imaging systems, US Patent 5577505, 26 November 1996.
- [66] V. Mor-Avi, E.G. Caiani, K.A. Collins, C.E. Korcarz, J.E. Bednarz, R.M. Lang, Combined assessment of myocardial perfusion and regional left ventricular function by analysis of contrast-enhanced power modulation images, *Circulation* 104 (3) (2001) 352–357.
- [67] B. Haider, R.Y. Chiao, Higher order nonlinear ultrasonic imaging, in: *IEEE Ultrasonics Symposium*, NV, USA, 1999.
- [68] M.R. Sprague, E. Cherin, D.E. Goertz, F.S. Foster, Nonlinear emission from individual bubble microbubbles at high frequencies, *Ultrasound Med. Biol.* 36 (2) (2010) 313–324.
- [69] B.L. Helfield, B.Y. Leung, X. Huo, D.E. Goertz, Scaling of the viscoelastic shell properties of lipid encapsulated microbubbles with ultrasound frequency, *Ultrasonics* 54 (2014) 1419–1424.
- [70] J. Sijl, E. Gaud, P.J.A. Frinking, M. Arditi, N. de Jong, D. Lohse, M. Versluis, Acoustic characterization of single ultrasound contrast agent microbubbles, *J. Acoust. Soc. Am.* 124 (4091) (2008).
- [71] S.M. van der Meer, B. Dollet, M.M. Voormolen, C.T. Chin, A. Bouakaz, N. de Jong, M. Versluis, D. Lohse, Microbubble spectroscopy of ultrasound contrast agents, *J. Acoust. Soc. Am.* 121 (2007) 648–656.
- [72] B.L. Helfield, D.E. Goertz, Nonlinear resonance behavior and linear shell estimates for Definity and Micromarker assessed with acoustic microbubble spectroscopy, *J. Acoust. Soc. Am.* 133 (1158) (2013).
- [73] J. Tu, J. Guan, Y. Qiu, T.J. Matula, Estimating the shell parameters of SonoVue microbubbles using light scattering, *J. Acoust. Soc. Am.* 126 (6) (2009) 2954–2962.
- [74] K. Chetty, E. Stride, C.A. Sennoga, J.V. Hajnal, R.J. Eckersley, High-speed optical observations and simulation results of SonoVue microbubbles at low-pressure insonation, *IEEE Trans. Ultrason. Ferroelectr. Freq. Control* 55 (6) (2008) 1333–1342.
- [75] K. Tsiglifis, N.A. Pelekasias, Nonlinear radial oscillations of encapsulated microbubbles subject to ultrasound: The effect of membrane constitutive law, *J. Acoust. Soc. Am.* 123 (2008) 4059–4070.
- [76] S. Sijl, B. Dollet, M. Overvelde, V. Garbin, T. Rozendal, N. de Jong, D. Lohse, M. Versluis, Subharmonic behavior of phospholipid-coated ultrasound contrast agent microbubbles, *J. Acoust. Soc. Am.* 128 (2010) 3239.
- [77] R. Williams, E. Cherin, T.Y.J. Lam, J. Tavakkoli, R.J. Zemp, F.S. Foster, Nonlinear ultrasound propagation through layered liquid and tissue-equivalent media: computational and experimental results at high frequency, *Phys. Med. Biol.* 51 (22) (2006) 5809–5824.
- [78] M. Emmer, H.J. Vos, A. van Wamel, D.E. Goertz, M. Versluis, N. de Jong, Clinical relevance of pressure-dependent scattering at low acoustic pressures, *Ultrasonics* 47 (2007) 74–77.
- [79] G. Renaud, J.G. Bosch, A.F.W. van der Steen, N. de Jong, Low-amplitude non-linear volume vibrations of single microbubbles measured with an “acoustical camera”, *Ultrasound Med. Biol.* 40 (6) (2014) 1282–1295.
- [80] C.F. Caskey, D.E. Kruse, P.A. Dayton, T.K. Kitano, K.W. Ferrara, Microbubble oscillation in tubes with diameters of 12, 25, and 195 microns, *Appl. Phys. Lett.* 88 (3) (2006) 033902.
- [81] N. Hosseinkhah, H. Chen, T.J. Matula, P.N. Burns, K. Hynynen, Mechanisms of microbubble-vessel interactions and induced stresses: A numerical study, *J. Acoust. Soc. Am.* 134 (2013) 1875–1885.
- [82] B.L. Helfield, B.Y.C. Leung, D.E. Goertz, The effect of boundary proximity on the response of individual ultrasound contrast agent microbubbles, *Phys. Med. Biol.* 59 (2014) 1721–1745.

- [83] S. Paul, D. Russakow, R. Nahire, T. Nandy, A.H. Ambre, K. Katti, S. Mallik, S. Sarkar, In vitro measurement of attenuation and nonlinear scattering from echogenic liposomes, *Ultrasonics* 52 (7) (2012) 962–969.
- [84] L. Xia, F. Karandish, K.N. Kumar, J. Froberg, P. Kulkarni, K.N. Gange, Y. Choi, S. Mallik, K. Sarkar, Acoustic characterization of echogenic polymersomes prepared from amphiphilic block copolymers, *Ultrasound Med. Biol.* 44 (2) (2018) 447–457.
- [85] J.J. Kwan, G. Lajoinie, N. de Jong, E. Stride, M. Versluis, C.C. Coussios, Ultrahigh-speed dynamics of micrometer-scale inertial cavitation from nanoparticles, *Phys. Rev. Appl.* 6 (4) (2016) 044004(1-8).
- [86] E. Cherin, J.M. Melis, R.W. Bourdeau, M. Yin, D.M. Kochmann, F.S. Foster, M.G. Shapiro, Acoustic behavior of *Halobacterium salinarum* gas vesicles in the high-frequency range: Experiments and modeling, *Ultrasound Med. Biol.* 43 (5) (2017) 1016–1030.
- [87] D. Maresca, A. Lakshmanan, A. Lee-Gosselin, J.M. Melis, Y.-L. Ni, R.W. Bourdeau, D.M. Kochmann, M.G. Shapiro, Nonlinear ultrasound imaging of nanoscale acoustic biomolecules, *Appl. Phys. Lett.* 110 (2017) 073704.
- [88] D. Maresca, D.P. Sawyer, G. Renaud, A. Lee-Gosselin, M.G. Shapiro, Nonlinear x-wave ultrasound imaging of acoustic biomolecules, *Phys. Rev. X* 8 (4) (2018) 041002.
- [89] J. Yan, M. Yin, F.S. Foster, C.E.M. Demore, Tumor contrast imaging with gas vesicles by circumventing the reticuloendothelial system, *Ultrasound Med. Biol.* 46 (2) (2020) 359–368.
- [90] M.A. Borden, G. Pu, G.J. Runner, M.L. Longo, Surface phase behavior and microstructure of lipid/PEG-emulsifier monolayer-coated microbubbles, *Colloids Surf., B* 35 (2004) 209–223.
- [91] G. Pu, M.A. Borden, M.L. Longo, Collapse and shedding transitions in binary lipid monolayers coating microbubbles, *Langmuir* 22 (7) (2006) 2993–2999.